

Non-contact rheology of finite-size air-water interfaces

Vincent Bertin,^{1,2,*} Zaicheng Zhang,^{1,*} Rodolphe Boisgard,¹ Christine Grauby-Heywang,¹ Elie Raphaël,² Thomas Salez,^{1,3,†} and Abdelhamid Maali^{1,‡}

¹*Univ. Bordeaux, CNRS, LOMA, UMR 5798, 33405 Talence, France.*

²*UMR CNRS Gulliver 7083, ESPCI Paris, PSL Research University, 75005 Paris, France.*

³*Global Station for Soft Matter, Global Institution for Collaborative Research and Education, Hokkaido University, Sapporo, Hokkaido 060-0808, Japan.*

(Dated: October 1, 2020)

We present non-contact atomic-force-microscopy measurements of the hydrodynamic interactions between a rigid sphere and an air bubble in water at the microscale. The size of the bubble is found to have a significant effect on the mechanical response due to the long-range capillary deformation of the air-water interface. We develop a viscocapillary lubrication model accounting for the finite-size effect that allows to rationalize the experimental data. This comparison allows us to measure the air-water surface tension, without contact and thus wetting, paving the way towards robust non-contact tensiometry of polluted air-water interfaces.

I. INTRODUCTION

The interface between two media has an energy cost per unit surface, called surface tension, resulting from the microscopic interactions of the constitutive molecules at the interface [1, 2]. Surface tension is an important parameter in soft condensed matter and at small scales where capillary phenomena usually dominate. Examples include wetting properties [3, 4], thin-film dynamics [5, 6], multiphase flows...

Surface active molecules – *i.e.* surfactants – are widely used to stabilize capillary interfaces on purpose, *e.g.* in emulsions or foams, but are also inevitable due to pollution. These particles, which are usually adsorbed at the interface between two immiscible liquids or between a liquid and a gas, lower the surface tension and are responsible for specific rheological properties of the interface [7]. To understand the dynamics of soft materials, the interaction between objects such as droplets and bubbles, or to quantify the amount of interfacial contamination, capillary interfacial rheology is essential. Specifically, surface tension is measured by a large variety of methods: using the energy minimization principle, via the pendant-drop method [8], or spinning-drop method, or measuring capillary forces with Wilhelmy plates or Du Noy rings [9], for instance. The interfacial rheology is usually determined with the Langmuir trough [10] or through oscillating-disk devices [11].

A complementary device to measure material properties is the atomic-force microscope (AFM), which has been recently used to study capillary phenomena such as the interaction between bubbles [12, 13] or droplets [14–16], the hydrodynamic boundary condition at a water-air interface [17, 18], and dynamical wetting [19–24]. Recently, the AFM has also been employed in a dynamical

mode, and appeared to be a remarkable tool to quantify mechanical properties with the advantage of providing non-contact measurements [25–29].

In this article, we study the force exerted on a water-immersed colloidal sphere attached to an AFM cantilever, that is driven to oscillate near the apex of an air bubble. The deformation of the bubble and the force exerted on the colloidal probe, are both coupled and due to the hydrodynamic pressure induced by the oscillating water flow. To rationalize the experimental data, we develop a lubrication model accounting for finite-size effects – which are found to be significant in the linear viscocapillary response. All together, this method allows for robust rheological measurements of the surface tension in the absence of any direct contact.

II. EXPERIMENTS

The experimental system is inspired by [18, 30]. Briefly, an air microbubble is generated in a sodium dodecyl sulfate (SDS) solution in water, of concentration C in the 0.2 – 40 mM range, at the tip of a syringe and deposited over a glass substrate precoated with a polystyrene layer. The bubble's curvature radius R_b and the contact angle, as measured with an optical microscope, are in the range 200 – 600 μm and 40 – 90°, respectively. Besides, a spherical particle, of radius $R_s = 54 \mu\text{m}$, is glued to the tip of an AFM cantilever and oscillates vertically at an imposed frequency $f = 100, 200, \text{ or } 300 \text{ Hz}$. The setup is sketched in Fig. 1. The instantaneous hydrodynamic force exerted on the particle is then measured for various sphere-bubble distances through the deflection of the AFM cantilever. The cantilever stiffness is calibrated using the drainage method and is equal to 0.249 N/m.

*These authors contributed equally.

†Electronic address: thomas.salez@u-bordeaux.fr

‡Electronic address: abdelhamid.maali@u-bordeaux.fr

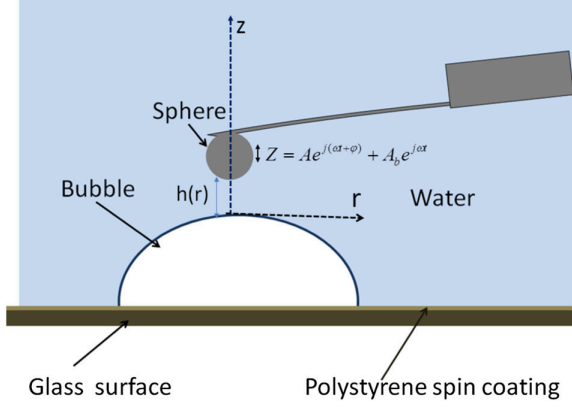


Figure 1: Schematic of the experimental setup. A spherical colloidal probe attached to an AFM cantilever oscillates vertically along z within water and near an air bubble. This results in an axisymmetric water gap thickness profile $h(r, t)$, varying with radial distance r and time t .

III. MODEL

We consider the asymmetric system composed of the rigid sphere located at an average distance D from the undeformed air bubble. The ensemble is immersed in an incompressible Newtonian fluid (water) of dynamical shear viscosity η . The sphere oscillates vertically at angular frequency $\omega = 2\pi f$ and with amplitude h_0 . The liquid gap thickness is denoted $h(r, t)$, with r the radial axis and t the time, and reads:

$$h(r, t) = D + \frac{r^2}{2R_{\text{eff}}} + h_0 \cos(\omega t) + u(r, t), \quad (1)$$

with $R_{\text{eff}}^{-1} = R_s^{-1} + R_b^{-1}$ the effective curvature. The field $u(r, t)$ denotes the vertical deformation of the air-water interfacial profile along $-z$, with respect to the equilibrium spherical-cap shape. We focus on the situation where the sphere-bubble distance is much smaller than the effective radius R_{eff} , so that we can invoke the lubrication approximation. The experiments are done at low enough frequency and with a non-zero surfactant concentration, so that we can assume a no-slip hydrodynamic boundary condition at the air-water interface [18]. Such a condition is also assumed at the sphere-water interface. Therefore, the liquid gap thickness follows the Reynolds equation:

$$\frac{\partial h(r, t)}{\partial t} = \frac{1}{12\eta r} \frac{\partial}{\partial r} \left[r h(r, t)^3 \frac{\partial}{\partial r} p(r, t) \right], \quad (2)$$

where $p(r, t)$ is the excess pressure field with respect to the atmospheric pressure. Since in the lubrication approximation the pressure is invariant along z , it can be evaluated at the air-water interface through the Laplace

law:

$$p(r, t) = \gamma \frac{1}{r} \frac{\partial}{\partial r} \left[r \frac{\partial u(r, t)}{\partial r} \right], \quad (3)$$

where γ denotes the air-water surface tension, and where small slopes were assumed. The contribution of Hamaker forces is neglected in the model as the typical sphere-bubble distance of interest in the experiment is 10 – 1000 nm which is larger than the distance below which these forces are dominant. The forcing amplitude h_0 is assumed to be small with respect to the sphere-bubble distance, so that we can treat p and u as perturbative fields, and linearize further Eq. (2). Introducing an harmonic decomposition, through $u(r, t) = \text{Re}[u^*(r)e^{i\omega t}]$ and $p(r, t) = \text{Re}[p^*(r)e^{i\omega t}]$, where Re denotes the real part and $u^*(r)$ and $p^*(r)$ are complex fields ($i^2 = -1$), Eq. (2) becomes:

$$12\eta r i \omega \left[h_0 + u^*(r) \right] = \frac{d}{dr} \left[r \left(D + \frac{r^2}{2R_{\text{eff}}} \right)^3 \frac{dp^*(r)}{dr} \right]. \quad (4)$$

Such a viscopillary problem is sensitive to the total size of the system, as in Ref. [15, 30] where it has been show that the central deformation diverges logarithmically with the system size. Therefore, it is necessary to introduce a cut-off radius b in the model. The excess pressure and the deformation fields are set to zero at radial distances larger than the cut-off radius, *i.e.*:

$$p^*(r) = 0, \quad u^*(r) = 0, \quad r > b. \quad (5)$$

We use the discrete Hankel transform to solve these equations. Both fields are expanded in terms of Fourier-Bessel series [31], for $r \in [0, b]$, as:

$$p^*(r) = \sum_{k=1}^{\infty} p_k J_0(\phi_k r), \quad u^*(r) = \sum_{k=1}^{\infty} u_k J_0(\phi_k r), \quad (6)$$

where J_0 is the Bessel function of the first kind with index 0, and $\phi_k = \mathcal{O}_k/b$ with \mathcal{O}_k the k th root of the Bessel function. The series coefficients are related to the deformation field via the inversion relation:

$$u_k = \frac{2}{b^2 J_1^2(\phi_k b)} \int_0^b u^*(r) J_0(\phi_k r) r dr, \quad (7)$$

where J_1 is the Bessel function of the first kind with index 1. We introduce the dimensionless variables:

$$x = \frac{r}{\sqrt{2R_{\text{eff}}D}}, \quad U^* = u^*/h_0, \quad P^* = \frac{p^*}{\frac{\eta R_{\text{eff}} h_0 \omega}{D^2}}, \quad (8)$$

$$B = \frac{b}{\sqrt{2R_{\text{eff}}D}}, \quad \psi_k = \phi_k \sqrt{2R_{\text{eff}}D},$$

such that Eqs. (4) and (3) respectively become:

$$24ix \left(1 + U^* \right) = \frac{d}{dx} \left[x \left(1 + x^2 \right)^3 \frac{dP^*}{dx} \right], \quad (9)$$

$$\frac{1}{8} \left(\frac{D_c}{D} \right) P^* = \frac{1}{x} \frac{d}{dx} \left(x \frac{dU^*}{dx} \right), \quad (10)$$

where $D_c = 16R_{\text{eff}}^2 \eta \omega / \gamma$ is a typical viscocapillary length that emerges from the rescaling. By integrating Eq. (9) with respect to x , and invoking the Fourier-Bessel decomposition, we find:

$$-x(1+x^2)^3 \sum_{k=1}^{\infty} \psi_k P_k J_1(\psi_k x) = 12ix^2 + 24i \sum_{k=1}^{\infty} U_k \frac{J_1(\psi_k x)}{\psi_k}, \quad (11)$$

where $U_k = u_k/h_0$ and $P_k = p_k D^2 / (\eta R_{\text{eff}} h_0 \omega)$. Using Eq. (10), one shows that the Fourier-Bessel coefficients U_k and P_k are related by:

$$\psi_k^2 U_k = \frac{1}{8} \left(\frac{D_c}{D} \right) P_k. \quad (12)$$

Injecting the last relation in Eq. (11), we find:

$$-\sum_{l=1}^{\infty} \psi_l P_l J_1(\psi_l x) = \frac{12ix}{(1+x^2)^3} + \frac{3i}{(1+x^2)^3} \left(\frac{D_c}{D} \right) \sum_{l=1}^{\infty} P_l \frac{J_1(\psi_l x)}{\psi_l^3} \text{ expansion, we finally get:} \quad (13)$$

We perform the Fourier-Bessel inversion by applying to Eq. (13) the operator $\frac{2}{B^2 J_1^2(\psi_k B)} \int_0^B y J_1(\psi_k y) (*) dy$, where $(*)$ stands for a function of y , and we find that the excess-pressure Fourier-Bessel coefficients satisfy:

$$P_k = A_k + \sum_{l=1}^{\infty} M_{k,l} P_l, \quad \forall k \in \mathbb{N}^*, \quad (14)$$

where A_k and $M_{k,l}$ are defined as:

$$A_k = -12i \frac{2}{B^2 J_1^2(\psi_k B)} \int_0^B \frac{y^2}{(1+y^2)^3} \frac{J_1(\psi_k y)}{\psi_k} dy, \quad (15)$$

and:

$$M_{k,l} = -3i \left(\frac{D_c}{D} \right) \frac{2}{B^2 J_1^2(\psi_k B)} \int_0^B \frac{y}{(1+y^2)^3} \frac{J_1(\psi_k y)}{\psi_k} \frac{J_1(\psi_l y)}{\psi_l^3} dy. \quad (16)$$

The vertical hydrodynamic force exerted on the sphere is $\int_0^b p(r, t) 2\pi r dr$ in dimensioned variables. We further define the complex mechanical impedance G^* as the ratio between the amplitude of the latter force and the driving amplitude h_0 [25]:

$$G^* = -\frac{1}{h_0} \int_0^b 2\pi r p^*(r) dr = -\frac{4\pi\eta\omega R_{\text{eff}}^2}{D} \int_0^B x P^*(x) dx. \quad (17)$$

Defining the dimensionless impedance $\mathcal{G}^* = G^* D_c / (6\pi\eta\omega R_{\text{eff}}^2)$, and invoking the Fourier-Bessel

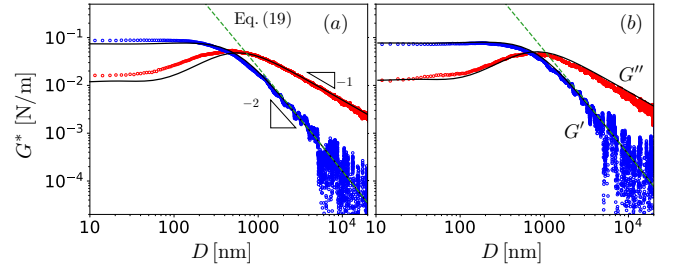


Figure 2: Complex mechanical impedance $G^* = G' + iG''$ versus sphere-bubble distance D for a SDS concentration of $C = 1$ mM, and excitation frequencies of: (a) $f = 200$ Hz, and (b) $f = 300$ Hz. The blue (resp. red) dots show the real G' (resp. imaginary G'') part. The results of the model (see Eq. (18)) are displayed with black solid lines and the asymptotic calculation at large distance (see Eq. (19) and Appendix) is shown with green dashed lines. The slope triangles indicate power-law exponents. The fitted surface tension value is $\gamma = 58$ mN/m.

$$\mathcal{G}^* = -\frac{4}{6} \frac{D_c}{D} \sum_{k=1}^{\infty} P_k \frac{B J_1(\psi_k B)}{\psi_k}. \quad (18)$$

To obtain the results presented in the following section, Eq. (14) is solved numerically with the 1000 first Fourier-Bessel modes, and the mechanical impedance is then computed from Eq. (18). We checked the robustness of the results against a change of the number of Fourier-Bessel modes used.

IV. RESULTS

In Fig. 2, we plot the mechanical impedance G^* versus the sphere-bubble distance D , for a SDS concentration of $C = 1$ mM, two driving frequencies and three bubble curvature radii. The complex impedance $G^* = G' + iG''$ is decomposed in its real (G') and imaginary (G'') parts. The results of the model are in good agreement with the experimental data. The air-water surface tension $\gamma = 58$ mN/m is the only fitting parameter in this comparison. We stress that, in the model, we used the half contour length of the undeformed air-water interface as a cut-off radius, *i.e.* $b = R_b (\pi - \theta)$, where θ denotes the contact angle.

Furthermore, two asymptotic regimes can be observed, with a crossover near $D \approx 1000$ nm that corresponds typically to D_c , equal to 727 and 1091 nm in Fig. 2(a) and (b), respectively. At large distance, we observe that the imaginary part of the mechanical impedance dominates and follows a $\sim D^{-1}$ scaling law, as expected from the asymptotic expression $G'' = 6\pi\eta R_{\text{eff}}^2 \omega / D$ [25]. The restoring capillary response of the air-water interface appears in the real part of G^* with an apparent $G' \sim D^{-2}$ scaling law at large distance. We stress that this is not

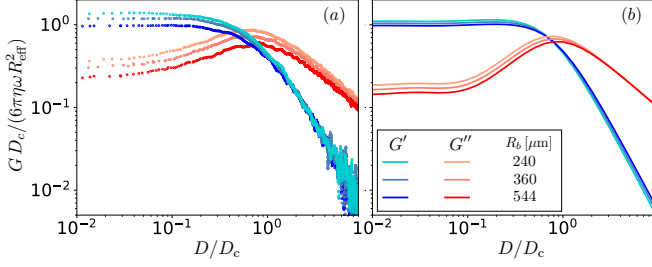


Figure 3: Dimensionless mechanical impedance versus dimensionless distance for 3 bubble sizes as indicated in the legend, with the same frequency $f = 200$ Hz, and a surfactant concentration $C = 1$ mM. The experimental data are shown in (a), and the results of the theoretical model are plotted in (b), using half the contour length as a cut-off size.

an exact scaling law, due to a logarithmic correction (see Appendix):

$$G'(D) \simeq \frac{9\pi\eta^2 R_{\text{eff}}^3 \omega^2}{\gamma D^2} \left[-1 + \log \left(1 + \frac{b^2}{2R_{\text{eff}} D} \right) \right]. \quad (19)$$

At small distance, both parts of the mechanical impedance saturate to constant values, and the storage component G' is larger than the loss one G'' . A similar saturation is also encountered in the elastohydrodynamic response near soft substrates [25–27] and is attributed to the fact that the deformation cannot exceed the excitation amplitude. As a consequence, the pressure saturates, so does the hydrodynamic force.

In order to test the ability of our model to account for the finite-size effects in the viscopillary response, we present in Fig. 3 the dimensionless mechanical impedance versus the rescaled distance for three bubble radii, ranging from $R_b = 240$ to $544 \mu\text{m}$, with the same driving frequency and surfactant concentration. The experimental curves are shown in Fig. 3(a), while the theoretical ones are shown in Fig. 3(b) where the cut-off radius is set to half the contour length of the undeformed air-water interface. Except for the loss component in the large-distance limit, the dimensionless mechanical impedance is generally found to depend on the bubble size in a non-trivial way, which is correctly reproduced by the model. This observation highlights the importance of finite-size effects in viscopillary settings. We note that the logarithmic correction in the large-distance expression of the dimensionless storage component (see Eq. (A5)) contains a bubble-size dependence which cannot be distinguished clearly with the AFM sensitivity given the bubble-size range. At small distance, the size dependence is more important and both the real and imaginary parts of the dimensionless mechanical impedance decrease with the bubble size.

Having discussed the finite-size effects in the global force response, we now illustrate them in Fig. 4 through the radial dependences of the local pressure and deformation fields. Specifically, we plot the complex dimen-

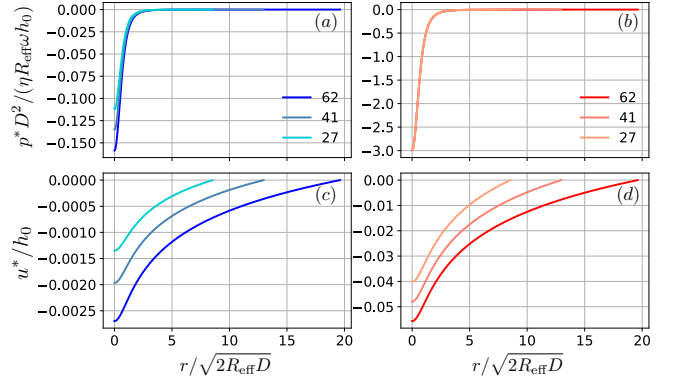


Figure 4: Real (a) and imaginary (b) parts of the dimensionless theoretical pressure field as functions of the dimensionless radial coordinate, at a dimensionless distance $D/D_c = 10$, for the three bubble radii of Fig. 3. The real and imaginary parts of the corresponding theoretical deformation field are plotted in (c) and (d), respectively.

sionless pressure and displacement fields versus the dimensionless distance, for the same cut-off radius as in Fig. 3, and at a fixed rescaled distance $D/D_c = 10$. We observe that both the real and imaginary parts of the dimensionless pressure field decay rapidly on a typical distance $\sim \sqrt{R_{\text{eff}} D}$. The imaginary part does not depend on the cut-off radius and is well described by the leading-order lubrication pressure in Eq. (A2). In addition, the real part does depend on the cut-off radius, through B , as predicted by the next-order correction in Eq. (A4). This dependence in B yields the logarithmic correction in the large-distance asymptotic expression of the storage component in Eq. (A5). In contrast with the dimensionless pressure field, the dimensionless deformation field depends on the cut-off radius. This is due to the long-range capillary deformation of the air-water interface, and is the reason why the finite-size effects are significant in viscopillary interactions.

So far, the air-water surface tension was considered as a free parameter and was fixed by fitting the AFM experimental data to the model. In the remaining, we discuss the capacity of our comparison method to be used as a robust tensiometer. In Fig. 5 is plotted the fitted surface tension as a function of the SDS concentration in water. We observe that the surface tension globally decreases with increasing surfactant concentration, as expected. At surfactant concentrations smaller than 1 mM typically, the surface tension is close to the 72 mN/m value for pure water. At large concentrations, the surface tension saturates to a value on the order of 30 mN/m. The critical micellar concentration of SDS in water is estimated to be around 8 mM [32, 33], which is typically the concentration above which the surface tension saturates in Fig. 5. The uncertainty on the fitted surface tension is on the order of ± 4 mN/m and may result from two main sources: i) the experiments at different frequencies lead to fitted values which vary by a few percents ;

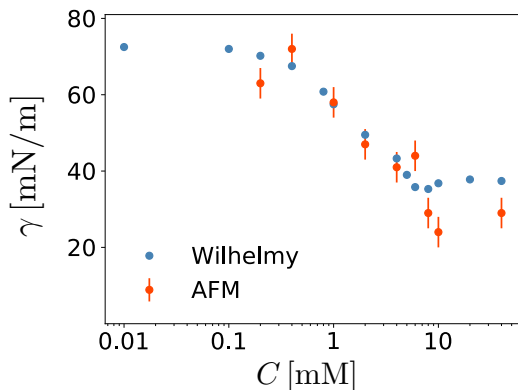


Figure 5: Air-water surface tension as a function of SDS concentration, as obtained from fits of the AFM data by the model (red dots). For comparison, independent measurements using the Wilhelmy-plate method are provided (blue dots).

ii) we take half the contour length of the undeformed air-water interface as a cut-off radius, while one could possibly make other choices, *e.g.* the curvature radius of the interface, which would modify slightly the fitted values. Finally, we performed independent tensiometry experiments on similar air-water-SDS interfaces using the Wilhelmy-plate method. The results are also shown in Fig. 5, and agree well with the ones obtained from the combination of our AFM measurements and model. Possible systematic deviations at the highest concentrations may result from micellar effects.

V. CONCLUSION

We studied the viscocapillary interaction between an air bubble and a spherical colloidal probe attached to an AFM cantilever, and immersed within a SDS solution in water. The sphere was oscillated in the direction normal to the air-water interface, thus generating a flow and an associated hydrodynamic pressure field that could deform the interface. The resulting force exerted on the sphere was measured as a function of the sphere-bubble distance, and found to depend on the bubble size. We developed a model, coupling axisymmetric lubrication flow and capillary deformations, and accounting for finite-size effects through a cut-off radial distance. The experimental results were found to be in good agreement with the model, assuming the cut-off radius to be half the contour length of the undeformed air-water interface, and with the air-water surface tension as a single free parameter. Finally, from a comparison with independent tensiometry measurements using the Wilhelmy-plate method, we discussed the capacity of our novel method to measure surface tensions robustly. This

work paves the way to non-contact capillary rheology with fundamental perspectives in confined soft matter, and practical applications towards water-contamination monitoring, to name a few.

VI. ACKNOWLEDGEMENTS

The authors thank Elisabeth Charlaix for preliminary discussions, as well as Samir Almohamad for technical assistance on the Wilhelmy-plate calibration experiments. Z. Z. acknowledges financial support from the Chinese Scholarship Council.

Appendix A: Asymptotic model at large distance

In this section, we derive an asymptotic solution, assuming that the ratio D_c/D is a small parameter, and we expend the excess pressure and field as:

$$P^*(x) \simeq P_0^*(x) + \frac{D_c}{D} P_1^*(x). \quad (\text{A1})$$

The leading-order pressure P_0^* is given by Eq. (9) in the undeformed-interface limit, and reads:

$$P_0^*(x) = -\frac{3i}{(1+x^2)^2}. \quad (\text{A2})$$

Similarly, the leading-order deformation U_1^* can be found by inserting P_0^* in Eq. (10) and invoking the boundary condition $U_1^*(x=B)=0$. We find:

$$U_1^*(x) = -\frac{3i}{32} \frac{D_c}{D} \left[\log(1+B^2) - \log(1+x^2) \right]. \quad (\text{A3})$$

Then, introducing U_1^* in Eq. (9) allows us to compute the next-order correction in pressure:

$$P_1^*(x) = \frac{3}{32} \left[-3 \frac{\log(1+B^2)}{(1+x^2)^2} - \pi^2 + \frac{3}{(1+x^2)^2} + \frac{3}{(1+x^2)} + 2 \frac{\log(1+x^2)}{1+x^2} - \log^2(1+x^2) - 2\text{Li}_2(-x^2) \right], \quad (\text{A4})$$

where Li_2 denotes the dilogarithm function [34]. After some algebra, we find that:

$$\mathcal{G}' = \text{Re}(\mathcal{G}^*) \simeq \frac{3}{32} \left(\frac{D_c}{D} \right)^2 \left[-1 + \log(1+B^2) \right], \quad (\text{A5})$$

which is equivalent to Eq. (19) with dimensioned variables.

-
- [1] P.-G. De Gennes, F. Brochard-Wyart, and D. Quéré, *Capillarity and wetting phenomena: drops, bubbles, pearls, waves* (Springer Science & Business Media, 2013).
- [2] A. Marchand, J. H. Weijs, J. H. Snoeijer, and B. Andreotti, *American Journal of Physics* **79**, 999 (2011).
- [3] P.-G. De Gennes, *Reviews of modern physics* **57**, 827 (1985).
- [4] D. Bonn, J. Eggers, J. Indekeu, J. Meunier, and E. Rolley, *Reviews of modern physics* **81**, 739 (2009).
- [5] A. Oron, S. H. Davis, and S. G. Bankoff, *Reviews of modern physics* **69**, 931 (1997).
- [6] R. V. Craster and O. K. Matar, *Reviews of modern physics* **81**, 1131 (2009).
- [7] D. Langevin, *Annual review of fluid mechanics* **46**, 47 (2014).
- [8] J. D. Berry, M. J. Neeson, R. R. Dagastine, D. Y. Chan, and R. F. Tabor, *Journal of colloid and interface science* **454**, 226 (2015).
- [9] J. Drelich, C. Fang, and C. White, *Encyclopedia of surface and colloid science* **3**, 3158 (2002).
- [10] D. K. Schwartz, C. M. Knobler, and R. Bruinsma, *Physical review letters* **73**, 2841 (1994).
- [11] P. Erni, P. Fischer, E. J. Windhab, V. Kusnezov, H. Stettin, and J. Läger, *Review of scientific instruments* **74**, 4916 (2003).
- [12] I. U. Vakarelski, J. Lee, R. R. Dagastine, D. Y. Chan, G. W. Stevens, and F. Grieser, *Langmuir* **24**, 603 (2008).
- [13] I. U. Vakarelski, R. Manica, X. Tang, S. J. O'Shea, G. W. Stevens, F. Grieser, R. R. Dagastine, and D. Y. Chan, *Proceedings of the National Academy of Sciences* **107**, 11177 (2010).
- [14] R. R. Dagastine, R. Manica, S. L. Carnie, D. Chan, G. W. Stevens, and F. Grieser, *Science* **313**, 210 (2006).
- [15] D. Y. Chan, E. Klaseboer, and R. Manica, *Soft Matter* **7**, 2235 (2011).
- [16] R. F. Tabor, F. Grieser, R. R. Dagastine, and D. Y. Chan, *Journal of colloid and interface science* **371**, 1 (2012).
- [17] O. Manor, I. U. Vakarelski, G. W. Stevens, F. Grieser, R. R. Dagastine, and D. Y. Chan, *Langmuir* **24**, 11533 (2008).
- [18] A. Maali, R. Boisgard, H. Chraïbi, Z. Zhang, H. Kellay, and A. Würger, *Physical Review Letters* **118**, 084501 (2017).
- [19] S. Ecke, M. Preuss, and H.-J. Butt, *Journal of adhesion science and technology* **13**, 1181 (1999).
- [20] X. Xiong, S. Guo, Z. Xu, P. Sheng, and P. Tong, *Physical Review E* **80**, 061604 (2009).
- [21] M. Delmas, M. Monthieux, and T. Ondarçuhu, *Physical review letters* **106**, 136102 (2011).
- [22] S. Guo, M. Gao, X. Xiong, Y. J. Wang, X. Wang, P. Sheng, and P. Tong, *Physical review letters* **111**, 026101 (2013).
- [23] J. Dupré de Baubigny, M. Benzaquen, L. Fabié, M. Delmas, J.-P. Aimé, M. Legros, and T. Ondarçuhu, *Langmuir* **31**, 9790 (2015).
- [24] C. Mortagne, K. Lippera, P. Tordjeman, M. Benzaquen, and T. Ondarçuhu, *Physical Review Fluids* **2**, 102201 (2017).
- [25] S. Leroy and E. Charlaix, *Journal of Fluid Mechanics* **674**, 389 (2011).
- [26] S. Leroy, A. Steinberger, C. Cottin-Bizonne, F. Restagno, L. Léger, and É. Charlaix, *Physical Review Letters* **108**, 264501 (2012).
- [27] R. Villey, E. Martinot, C. Cottin-Bizonne, M. Phaner-Goutorbe, L. Léger, F. Restagno, and E. Charlaix, *Physical Review Letters* **111**, 215701 (2013).
- [28] D. Guan, C. Barraud, E. Charlaix, and P. Tong, *Langmuir* **33**, 1385 (2017).
- [29] Z. Zhang, V. Bertin, M. Arshad, E. Raphaël, T. Salez, and A. Maali, *Phys. Rev. Lett.* **124**, 054502 (2020).
- [30] Y. Wang, B. Zeng, H. T. Alem, Z. Zhang, E. Charlaix, and A. Maali, *Langmuir* **34**, 1371 (2018).
- [31] G. N. Watson, *A treatise on the theory of Bessel functions* (Cambridge university press, 1995).
- [32] Y. Moroi, K. Motomura, and R. Matuura, *Journal of Colloid and Interface Science* **46**, 111 (1974).
- [33] E. Fuguet, C. Ràfols, M. Rosés, and E. Bosch, *Analytica Chimica Acta* **548**, 95 (2005).
- [34] M. Abramowitz and I. A. Stegun, *Handbook of mathematical functions with formulas, graphs, and ma* vol. 55 (US Government printing office, 1948).